Optics & Laser Technology 196 (2026) 114731

Contents lists available at ScienceDirect

Optics and Laser Technology

journal homepage: www.elsevier.com/locate/optlastec

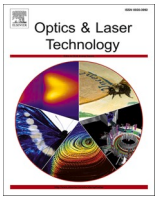

Parallel high-throughput system for time domain diffuse optical spectroscopy based on a 16-channel SiPM array☆

Elisabetta Avanzi [a,1], Giulia Maffeis [a,1,*], Nicola Serra [a], Alessandro Bossi [a,b], Valerio Gandolfi [a], Xinqiu Ye Lin [a], Andrea Farina [c], Cosimo D'Andrea [a], Laura Di Sieno [a], Paola Taroni [a,c], Antonio Pifferi [a,c], Alberto Dalla Mora [a]

[a] Dipartimento di Fisica, Politecnico di Milano, Milan, Italy
[b] Dipartimento di Meccanica, Politecnico di Milano, Milan, Italy
[c] Istituto di Fotonica e Nanotecnologie, Consiglio Nazionale delle Ricerche, Milan, Italy

ARTICLE INFO

Keywords:
Time domain
Diffuse optical spectroscopy
Spectral parallelization
Multi-channel detector
SiPM array
High-throughput
In vivo scan

ABSTRACT

The multi-channel SiPM technology is a fascinating leverage for time-resolved diffuse optical spectroscopy thanks to its remarkable parallelization capability that leads to rapidly measuring absorption and scattering properties of a turbid medium at multiple positions across a wide spectral range (600–1000 nm) at high throughput.

For clinical applications, where the goal is to characterize the composition of biological tissues (*e.g.*, fat, muscle, bone) *in vivo* non-invasively, these requirements are critical to support diagnosis with quantitative data, potentially reducing invasive procedures like biopsies and shortening waiting times for clinical exams.

Therefore, we developed a time domain diffuse optical spectroscopy (TD-DOS) system based on a compact 16-channel Silicon PhotoMultiplier (SiPM) array (footprint of 32 x 45 mm^2, with single-photon timing resolution of 65 ps), capable of spectral or spatial parallelization. Spectral parallelization enables swift acquisition of extensive spectra, for example during functional tasks, allowing monitoring of task-related tissue changes and minimizing exam duration without compromising the informative content. Spatial parallelization facilitates tissue mapping or deep-layer investigation by leveraging the relationship between source-detector separation and penetration depth that holds when operating in the time domain.

In this work, our system was configured to parallelize wavelengths across the 700–950 nm range (spectral resolution $\Delta\lambda = 16$ nm) to match key absorption peaks of hemoglobin and lipids, and the rising edge of water (peaking at 975 nm). Performance was evaluated applying the MEDPHOT protocol on phantoms, showing excellent linearity (worst $R^2 = 0.9973$ for absorption and $R^2 = 0.9833$ for reduced scattering), minimal absorption–scattering coupling, and remarkable absorption accuracy (average error of 3 % on absolute values), though scattering was overestimated (average error of + 17 %). *In vivo* trials demonstrated excellent reproducibility (CV < 5 % for absorption and < 4.5 % for scattering over 20 repetitions) and effective characterization of tissue during scans of the back and calf, correlating well with complementary ultrasound information about fat, muscle and bone layering.

This system combines for the first time to our knowledge time domain insights, SiPM robustness, and parallelization speed, paving the way for efficient sample characterization in clinical and non-clinical contexts.

1. Introduction

When evaluating the efficiency of devices, speed, robustness and cost-effectiveness are important requirements, alongside accuracy, repeatability and reliability. With reference to diffuse optical spectroscopy [1,2], this translates into the possibility to perform highly

☆ This article is part of a special issue entitled: 'Photonic Materials and Devices' published in Optics and Laser Technology.

* Corresponding author.
E-mail address: giulia.maffeis@polimi.it (G. Maffeis).

[1] These authors contributed to the work equally.

https://doi.org/10.1016/j.optlastec.2026.114731
Received 3 March 2025; Received in revised form 9 December 2025; Accepted 9 January 2026
Available online 14 January 2026
0030-3992/© 2026 The Authors. Published by Elsevier Ltd. This is an open access article under the CC BY license (http://creativecommons.org/licenses/by/4.0/).

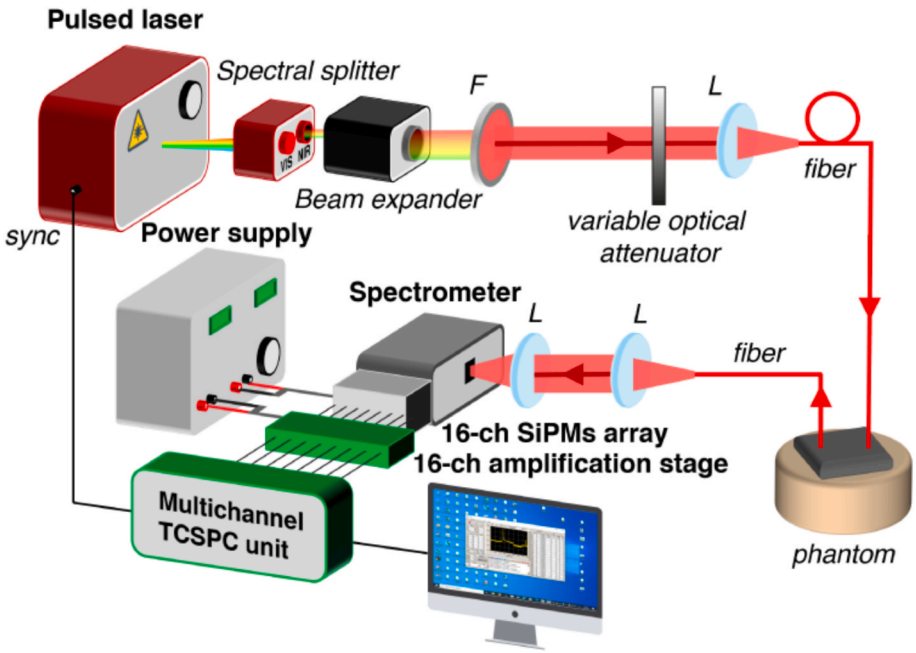

Fig. 1. Experimental setup scheme. F stands for filter, L for lens, TCSPC for Time-Correlated Single-Photon Counting.

informative measurements about the absorption and scattering properties of a turbid medium to describe its composition and microstructure quickly, operating at multiple wavelengths in the red and near-infrared spectral range (*e.g.*, 600–1100 nm) and at various positions. Results should have an adequate signal-to-noise ratio with minimal risk of instrument damage caused from unwanted light exposure, and acquisition should allow for repetition as often as needed, as the examination is affordable.

These requirements become especially important in clinical applications, for a seamless integration into the diagnostic workflow. In that case, the sample is a biological tissue (*e.g.*, fat, muscle, bone), measurements are performed *in vivo* with no harm to the subject and the goal is to help formulate a diagnosis or assist monitoring based on the estimate of tissue composition, mainly in terms of water, lipids, collagen, oxy- and deoxy-hemoglobin. The ultimate long-term benefit is to corroborate diagnosis (*e.g.*, breast lesion classification and therapy monitoring [3–6], muscle rehabilitation [7–10], brain activity monitoring [11–14], lung sensing [15]) with quantitative objective parameters elaborated in real-time, thus enabling a reduction in the number of invasive exams (*e.g.*, biopsies) and shorter waiting lists.

In this direction, we developed and preliminarily validated a time domain diffuse optical spectroscopy system based on a 16-channel Silicon PhotoMultiplier (SiPM) array. This device leverages its parallelization capabilities for various applications. In the context of clinical use, it can parallelize acquisition spectrally, to obtain fast extensive spectra for example during the monitoring of a functional task without interlacing the spectrum acquisition and the task evolution, or to minimize the exam duration for a fast tissue assessment. It can also parallelize acquisition spatially, to generate maps of tissue properties, or to investigate in depth multi-layered structures at different source-detector distances, given the correlation between penetration depth and injection-collection separation [16]. Previously, the device demonstrated potential for fluorescence lifetime sensing in biological applications [17]. In this work, we focus on the spectral parallelization over the 700–950 nm range to perform scanning measurements in a clinical environment. We present the system and the results of its performance evaluation on tissue phantoms. Then, we validate it *in vivo* performing scans along the back and around the calf, heterogeneous regions where muscle, fat and bones layers are present.

Systems already exist that achieve separately:

- robustness and high-throughput exploiting SiPMs for detection [18–20];
- high informative content through a time-resolved approach [21];
- parallelization with 16-channel detection [6,22–29];
- fast acquisition to monitor functional task by means of spectral parallelization [30–36].

Furthermore, combinations of these features already exist, specifically systems (even if rare) based on time-resolved approach, 16-channel detection and spectral parallelization [30–34]. However, those systems use bulky (*i.e.*, neither scalable nor miniaturized) Photo-Multipliers Tubes for detection, characterized by limited throughput and high sensitivity to stray light, less suitable for operation in clinical settings. To our knowledge, the system we propose is the first ever combination of time-resolved approach, spectral parallelization, 16-channel detection, and use of SiPMs for detection.

2. Setup Description and calibration

2.1. 16-channel SiPM array

The core element of the parallel system is the 16-channel array detector. It comprises independent detection channels, each featuring a front-end circuit designed to handle both biasing and signal read-out tasks. The biasing functionality provides the required voltage, suppresses high-frequency noise, and isolates the power supply from the circuit. The read-out section, implemented as a high-pass filter, facilitates rapid signal recovery to ground with minimal amplitude loss, enabling quick detection of consecutive events with just a 3.6 ns dead time between 2 consecutive events on the same detector. This enables us to operate in single-photon regime as required by TD-DOS.

The design emphasizes compactness (each single channel is 4×22.5 mm^2) and directs light dispersion along a single axis, in a linear configuration (the overall footprint of the printed circuit board hosting the array is 32 x 45 mm^2). Each channel integrates a 1.3×1.3 mm^2 active-area Silicon Photomultiplier (SiPM, model S13360-1350PE, Hamamatsu, Japan), which operates at a bias voltage of 57.3 V. The

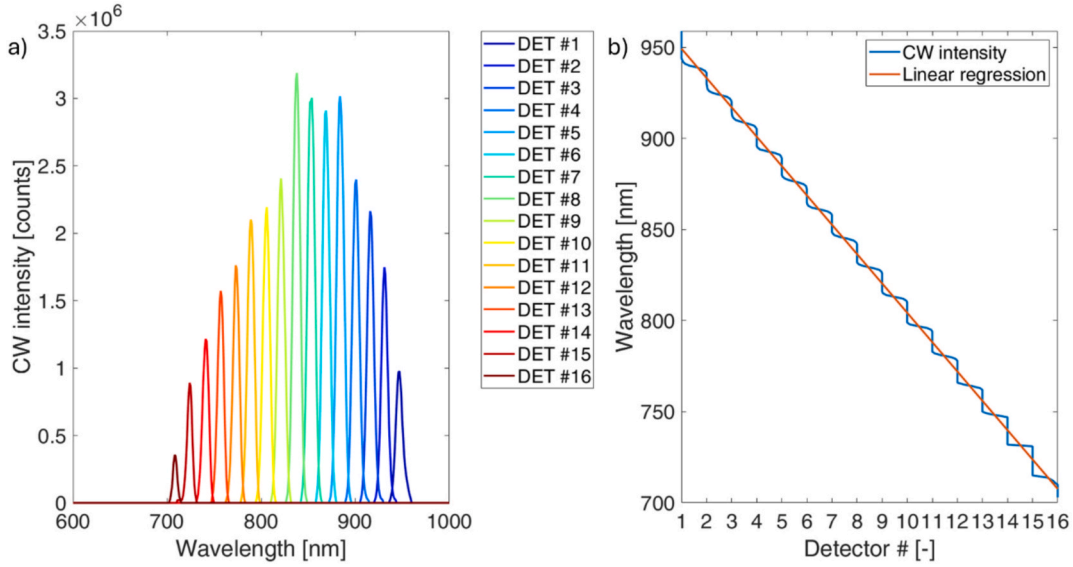

Fig. 2. A) signal intensity vs wavelength. cw stands for "continuous wave"; b) wavelength vs barycenter position, assessed in terms of detector number.

SiPM exhibits a dark count rate of almost 144 kcps and achieves a single-photon timing resolution of 65 ps. To align with the input requirements of commercial timing electronics, the array is complemented by a custom low-noise 16-channel amplification stage.

2.2. Experimental setup

The parallel system (Fig. 1) exploits a supercontinuum pulsed laser (SuperK Extreme, NKT Photonics, Denmark) to generate white light, operating at 40 MHz. To select wavelengths within the therapeutic window (600–1000 nm), the laser output is passed through a spectral splitter (SpectraK Split, NKT Photonics, Denmark) that isolates the near infrared band. A beam expander is used to avoid damage to the following band-pass filter, that further removes components longer than 1000 nm (FESH1000, Thorlabs, USA). A variable optical attenuator (variable neutral density filter) modulates light intensity and a lens couples light into the launch fiber (step index, 1 mm core diameter, NA = 0.39). The launch and collection fibers are arranged 2 cm apart in a hand-held probe. The collection fiber (step index, 500 μm core diameter, NA = 0.22) delivers light from the sample to a pair of lenses (25 and 50 mm focal length) that help matching the numeric aperture of the fiber with that of the spectrometer. The spectrometer (Kymera 193i, Oxford Instruments, Andor, UK) is configured to operate from 700 to about 950 nm and the dispersed light is collected by the 16-channel array detector. The amplified SiPM array output signals are sent to a 16-channel high-throughput time-to-digital converter (MultiHarp 160 N, PicoQuant, Germany – MH) for the Distributions of Times-Of-Flight (DTOF) reconstruction, with a time resolution of 5 ps on 5000 time bins.

2.3. Spectral calibration

The width and position of the spectral range depend on the diffraction grating of the spectrometer. For this work, we decided to use a diffraction grating with 600 grooves/mm and a central wavelength of 825 nm, thus spanning from 700 to 950 nm to match peculiar absorption features of lipids, water and hemoglobin in the therapeutic window [37].

The spectral resolution of the parallel system is determined by the detection chain. We expect each channel (*i.e.*, each SiPM of the array) to encompass a band of about $\Delta\lambda = \frac{950\ \text{nm}-700\ \text{nm}}{16\ \text{channels}} = 16$ nm. To determine the barycenter wavelength (*i.e.*, the leading wavelength) of each channel, acquisitions injecting single wavelengths with fine step increments are required. Therefore, measurements at 1 nm-steps at fixed attenuation were carried out with a hybrid setup that combined the collection chain of the parallel system and the injection chain of a well-characterized time-resolved system, based on a supercontinuum source and on a rotating prism for sequential wavelength selection [38], which has a spectral bandwidth of approximately 4 nm in the range of interest.

Table 1
Barycenter wavelength for each channel (#1 to #16), expressed in nm.

#1	#2	#3	#4	#5	#6	#7	#8
949	933	917	901	885	869	853	837
#9	**#10**	**#11**	**#12**	**#13**	**#14**	**#15**	**#16**
820	804	788	772	756	740	724	708

SiPMs exhibit significant dark noise, which was duly accounted for during data analysis. Noise subtraction (estimated as average noise level in the DTOF as it is impossible to remove individual dark noise events) was applied prior to any data processing.

For each channel, the DTOFs were summed over the time dimension to obtain a CW (Continuous Wave) intensity value for each wavelength. The result is depicted in Fig. 2a.

Then, the barycenter channel was computed for each wavelength, leading to the plot in Figs. 2b, and a linear regression yielded the values reported in Table 1.

On one side, the linear regression grants an equally spaced separation between spectral bands. On the other side, it allows one to decouple the barycenter computation from the signal intensity. In other words, this method is robust even changing the attenuation via the neutral density filter. It is good laboratory practice to repeat the spectral calibration at every measurement campaign. While the calibration discussed here above was used for the MEDPHOT protocol (see next section), a new one was applied to the *in vivo* measurements. The outcomes were very similar (minimum–maximum deviation in wavelength of 0–5 nm, compatible with the spectral resolution of the pulsed laser), but the use of a dedicated calibration warrants best performance.

It is worth mentioning that alternative configurations are also possible.

Using the same diffraction grating (thus maintaining a 250 nm span), the central wavelength can be shifted as desired. For instance, setting it to 725 nm would cover the 600–850 nm range, which is particularly suitable for hemodynamic studies.

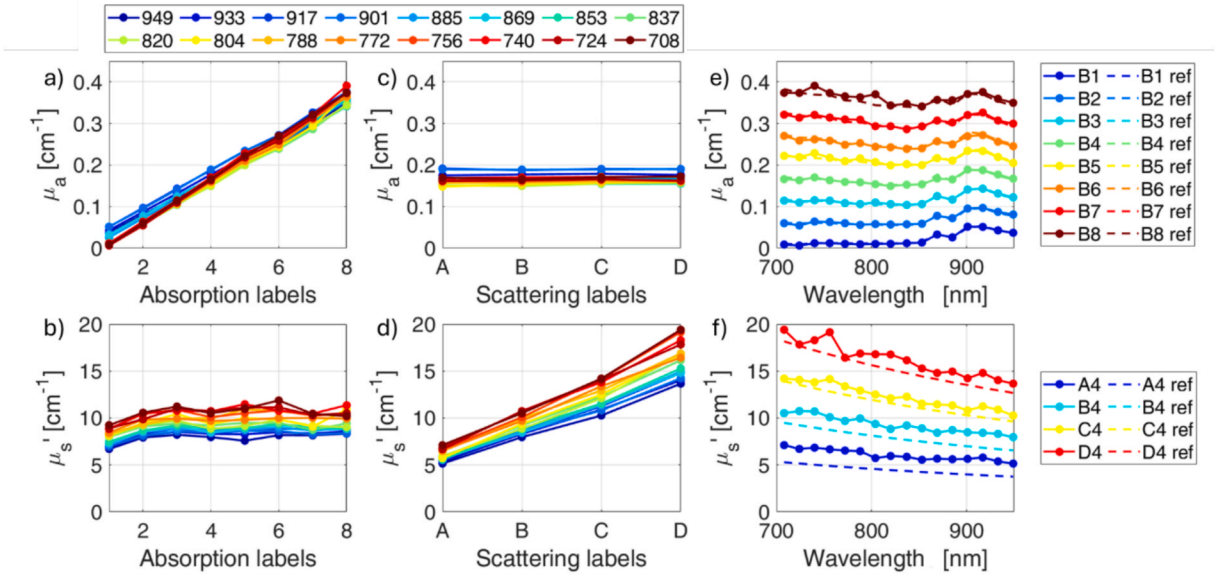

Fig. 3. Results for the linearity test of the MEDPHOT protocol (panels a-d) and absorption (e) and reduced scattering (f) spectra of resin phantoms. Panels a, b and e are referred to the "B" series of phantoms, while panels c, d and f to the "4" series. Labels on the top refer to the measurement wavelengths (nm) for data shown in panels a-d, while labels on the right identify the phantoms corresponding to spectra shown in panels e-f.

Alternatively, one can keep the same central wavelength (around 825 nm) and replace the diffraction grating to modify the spectral span: using a grating with a lower groove density broadens the range (at the cost of a worst spectral resolution), while a higher groove density narrows it (but improves the spectral resolution). Thus, a proper choice of the grating could allow either the inclusion of additional absorption peaks (*e.g.*, water at 975 nm, collagen at 1060 nm) or focusing on a specific one.

Both grating and central wavelength can also be adjusted simultaneously to tailor the spectral range width and position to a specific application. In all cases, setup constraints and application requirements must be considered. For example, SiPM efficiency remains adequate between 300 and 1100 nm (at most) and TD-DOS is usually interested to the 600–1100 nm window.

3. Performance evaluation

3.1. MEDPHOT protocol on phantoms

The MEDPHOT protocol is a standardized procedure for the performance assessment of diffuse optics instruments [39]. Linearity and accuracy are the two most informative tests of the protocol, since they describe the ability to track variations in the optical properties of the sample and quantify them correctly, which is key for correct diagnosis in clinical settings. The samples are homogeneous epoxy resin phantoms, labelled with a letter to identify the "conventionally true" reduced scattering (A: $\mu_s' = 5$ cm^{-1}, B: $\mu_s' = 10$ cm^{-1}, C: $\mu_s' = 15$ cm^{-1}, D:, $\mu_s' = 20$ cm^{-1}, at 800 nm) and a number for the absorption coefficient (1: $\mu_a = 0.05$ cm^{-1}, 2: $\mu_a = 0.1$ cm^{-1}, 3: $\mu_a = 0.15$ cm^{-1}, 4: $\mu_a = 0.2$ cm^{-1}, 5: $\mu_a = 0.25$ cm^{-1}, 6: $\mu_a = 0.3$ cm^{-1}, 7: $\mu_a = 0.35$ cm^{-1}, 8: $\mu_a = 0.4$ cm^{-1}, at 800 nm). Then, optical properties assume specific values according to the wavelength around the conventionally true value. Fig. 3 represents a subset of the possible combinations.

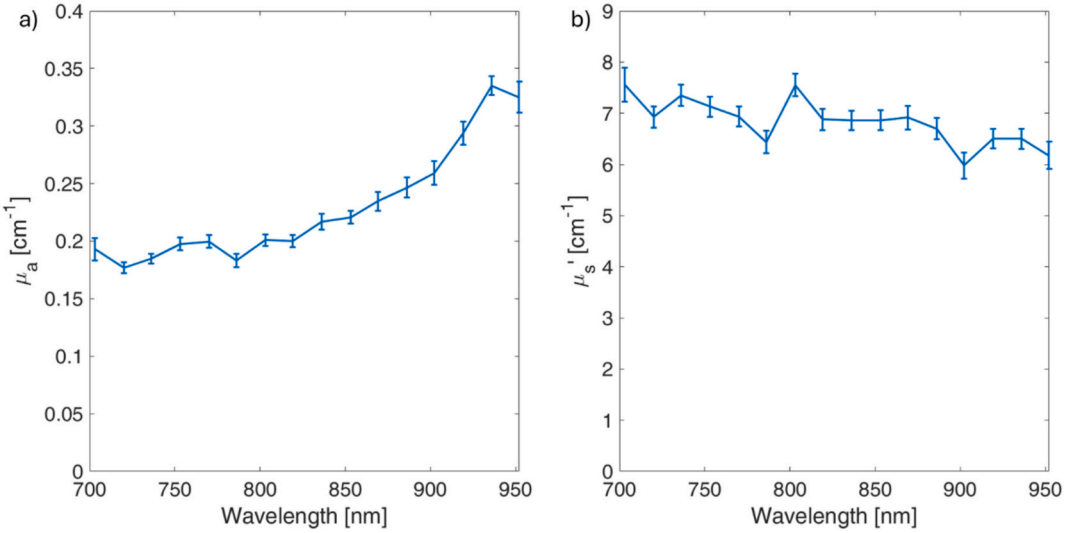

Fig. 4. Absorption (a) and reduced scattering (b) spectra (average and standard deviation) from static *in vivo* acquisitions on the forearm.

Ten repetitions of 1 s each were acquired at a source-detector distance of 2 cm. To extract the optical properties, DTOFs were fitted after noise subtraction using the analytical model for photon transport in a turbid semi-infinite medium under the diffusion approximation. The theoretical curve was convolved with the IRF to take into account the non-idealities of the system [40].

The system shows excellent linearity and negligible coupling between absorption and scattering (Fig. 3). In fact, the worst linear coefficients in Fig. 3a and Fig. 3d are $R^2 = 0.9973$ at 708 nm for absorption and $R^2 = 0.9833$ at 820 nm for scattering. The worst angular coefficients in absolute value for the ideally horizontal lines in Fig. 3b and Fig. 3c are 5.15 at 788 nm and < 0.01 at 804 nm, respectively. As an example, this implies that a 1-cm^{-1} effective increase in absorption could result in an unintended increase of 5.15 cm^{-1} in the measured scattering. Rescaled to our application, this corresponds to an undesired variation of 0.23 cm^{-1} in scattering for a 0.05 cm^{-1} change in absorption.

Comparing these results with the performance of the other 30 systems assessed under the same conditions (as summarized in Table 4 of Ref. [41]), the parallel system falls within the first quartile for the linearity in absorption (1.46 % – Fig. 3a), the second quartile for the linearity in scattering (3.7 % – Fig. 3d), the first quartile for the crosstalk on absorption (0.9 % – Fig. 3c) and the second quartile for the crosstalk on scattering (4.5 % – Fig. 3b). This is compliant with better performances in absorption rather than scattering previously discussed. The four mentioned panels shown in Fig. 4 illustrate a single series; however, the figure of merit was evaluated using all series, as described in Ref. [41].

To measure accuracy, a comparison between the parallel system and the values provided by a well-characterized time-resolved spectroscopy system [38] is shown in Fig. 3e and Fig. 3f. The comparison highlights an excellent match for absorption (average relative error on absolute value of 3 %), while scattering values tend to be overestimated (average of + 17 %). The retrieval of microstructure information is prone to errors because it is linked to scattering, but the absorption measurement is accurate and ensures a reliable tissue composition assessment, which is a critical factor for diagnostic applications. These results compare well with the performance of other photon migration instruments [41].

3.2. *In vivo reproducibility upon repositioning*

The *in vivo* assessment began with static tests to verify the reproducibility in repositioning the probe. If the coefficient of variation (CV, *i.e.*, the ratio between standard deviation and mean) is sufficiently small over 20 repetitions on the same location, then we are confident enough that variations in optical properties detected by the system are due to actual variations in tissue composition and not to experimental errors.

Measurements (20 repetitions of 1 s each) were taken at the midpoint of the forearm anterior part, where ulna is covered by a layer of fat and muscle, as hinted by the growth in absorption in Fig. 4a for wavelengths longer than 800 nm. The reduced scattering coefficient Fig. 4b slowly decreases from 700 to 950 nm, though the trend is not perfectly smooth, deviating from the clean exponential trend predicted by Mie theory. This is consistent with observations made on the homogeneous phantoms. The corresponding CVs are respectively lower than 5 % and 4.5 %, demonstrating a reliable tissue characterization.

4. Application for scanning *in vivo* measurements

4.1. *In vivo protocol for scanning measurements*

The system was devised to perform quick multi-wavelength acquisitions for a timely assessment of tissue composition. Three heterogeneous body parts were chosen, featuring varying thicknesses of fat and muscle layers, occasionally interrupted by bone: 1) the back, horizontally from left hip to right hip in the lumbar region crossing the spine, 2) the back in the lumbar region on the left side scanning vertically downwards, 3) the left calf, scanning clockwise from 6 to 3 o' clock across the tibia.

Table 2
Demographics of recruited subjects. BMI stands for body mass index.

	Age (y)	**Sex**	**BMI** (kg/m^2)	**Sport** (hours/week)
Subject 1	30	F	21.2	1–2
Subject 2	26	M	24.1	6–7
Subject 3	27	F	21.5	1–2

The parallelization of wavelength acquisition allows for swift moving measurements, with an operator holding the probe, similar to clinical ultrasound (US) imaging procedures. A linear grid of 21 points (from 0 to 20), in 1 cm steps, was drawn on the skin to guide the operator during scans. The only exception was a 1.5 cm spacing for subject 2 on the calf to accommodate its size. The source-detector axis of the probe was oriented perpendicular to the grid. Measurements were conducted in two modes: at discrete steps, with the probe held still at each position for a duration dictated by a metronome (5 acquisition repetitions of 1 s per position), and continuously, with the probe moving smoothly across the grid points, synchronized with the metronome timing. Probe sliding on the skin was favoured by the use of optically-tested ultrasound gel [42]. In both modalities, each point consists of 1 s of acquisition and about 1 s of dead time due to data transfer and processing. The duration of each scan was of about 8 min (21 positions x 5 repetitions x 2 s + 5 min probe positioning) for the discrete mode and about 40 s for the continuous mode. For discrete measurements, light attenuation was tuned at each position to optimize signal-to-noise ratio (17–20 Mcps over the 16 channels of the TCSPC board), while during continuous scans it was kept constant (15–25 Mcps over the 16 channels of the TCSPC board). The discrete measurement is used as optical ground truth with minimized motion artefacts. For all measurements, the subject was seated, with the leg resting on a stool at the same height as the seat only during the calf measurement.

Optical measurements were followed by B-mode US imaging (E2 Exp., Sonoscape Medical Corp., China) to assess the muscle and fat thicknesses and identify bone position. This information is used as ground truth to interpret and validate optical data.

Three subjects were measured, whose demographics is reported in Table 2. All measurements were approved by the Ethical Committee of Politecnico di Milano and performed after written informed consent.

Results were derived by replacing the Lambert-Beer law and an empirical approximation to Mie theory [40] into the solution of the diffusion equation for a homogeneous semi-infinite medium, with extrapolated boundary conditions [43]. Composition was assessed in terms of lipids, water, hemoglobin concentrations and oxygen saturation (estimated from oxy- and deoxyhemoglobin content). Microstructure was assessed in terms of scattering parameters: the scattering amplitude a is linked to the size of scattering centers and the scattering power b to their density, as envisioned by the Mie theory [44].

4.2. *Results and discussion for tissue characterization*

The following figures depict the results of *in vivo* scanning measurements. Fig. 5, Fig. 7 and Fig. 9 depict the optical results. Fig. 6, Fig. 8 and Fig. 10 depict the corresponding US images. The aim of US images is to show the stratified structure of the back and the calf, which consist of skin, fat, muscle and bone. The yellow lines indicate the fat thickness, which is the intermediate layer between the skin and the muscle/bone. The goal is to identify correlations between optical data and tissue structured imaged by US and show that the thicker the fat, the lower the contribution of muscle and bone in the tissue composition assessment.

Fig. 6 represents the spatial evolution across the back, passing through the spine. All curves regarding composition are symmetrical, with the central position as either the maximum or minimum. In

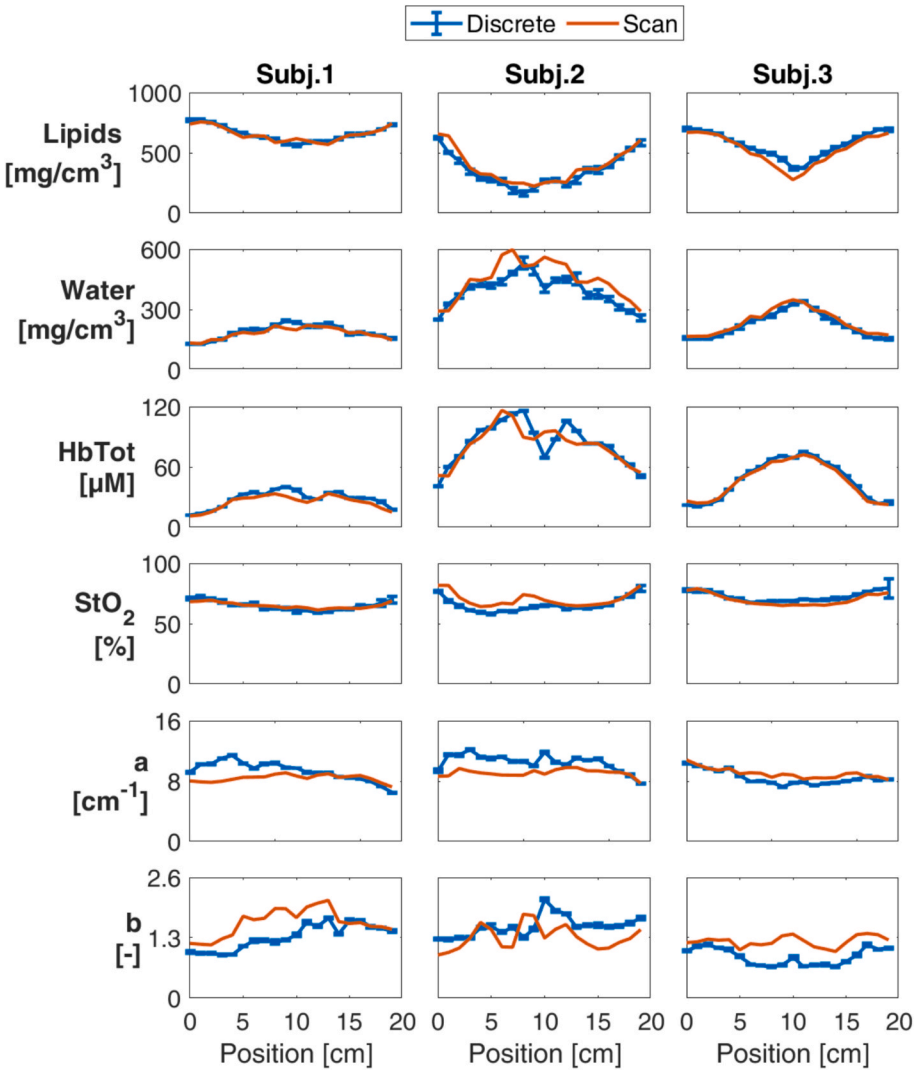

Fig. 5. Spatial variation of tissue composition for horizontal *in vivo* measurements across the back. Columns correspond to different subjects and rows to constituent concentrations and scattering parameters. Error bars represent the standard deviation over 5 repetitions of discrete acquisitions.

general, as shown by the US images in Fig. 6, on the hips the superficial adipose tissue in thicker and leads to a higher lipid content assessed optically, while, when approaching the spine, muscle (with high water and blood content) is closer to the surface and better probed by the optical measurements. The bone is a discontinuity point for the muscle layer (but not for the adipose one), with diverse effects. In fact, discrete and continuous acquisitions always yield consistent results, except for water and hemoglobin in subject 2 at the midpoint, where a sudden trend inversion is exhibited by the discrete mode. Subject 2 is a male with significantly thicker muscle layer than the two female subjects (in agreement with his higher water and blood content) and the different tissue structure might explain the results, where the spine clearly separates the left and right muscles (Fig. 6, position 10). Finally, it is worth mentioning that in all subjects oxygen saturation has an opposite behavior with respect to total hemoglobin, suggesting that oxyhemoglobin varies less significantly than deoxy-hemoglobin with position.

Fig. 7 illustrates the vertical distribution of lipids, water, hemoglobin, blood oxygen saturation and scattering parameters along the lumbar region of the back. As expected, in this situation there is no significant contribution from bones and a progressive increase is observed in fat tissue at the expense of muscle when approaching the hips. This trend is more marked in females than in males, not only in relative values but also in absolute ones, in agreement with what shown by the US images in Fig. 8 and what reported in general in the literature when sexes are compared [45]. Similar to what discussed about the previous measurements, here again the scattering parameters show no clear changes with position. The scattering slope seems to decrease with position in subject 1, but this is not confirmed in the other subjects.

Finally, Fig. 9 presents the results for circular scans around the calf. This is the most difficult measurement to perform given the surface curvature, which probably explains the less effective overlap between discrete and continuous acquisitions, and in particular the shift observed between the two acquisition modalities for subject 2. This notwithstanding, all measurements exhibit peaks and/or dips in correspondence

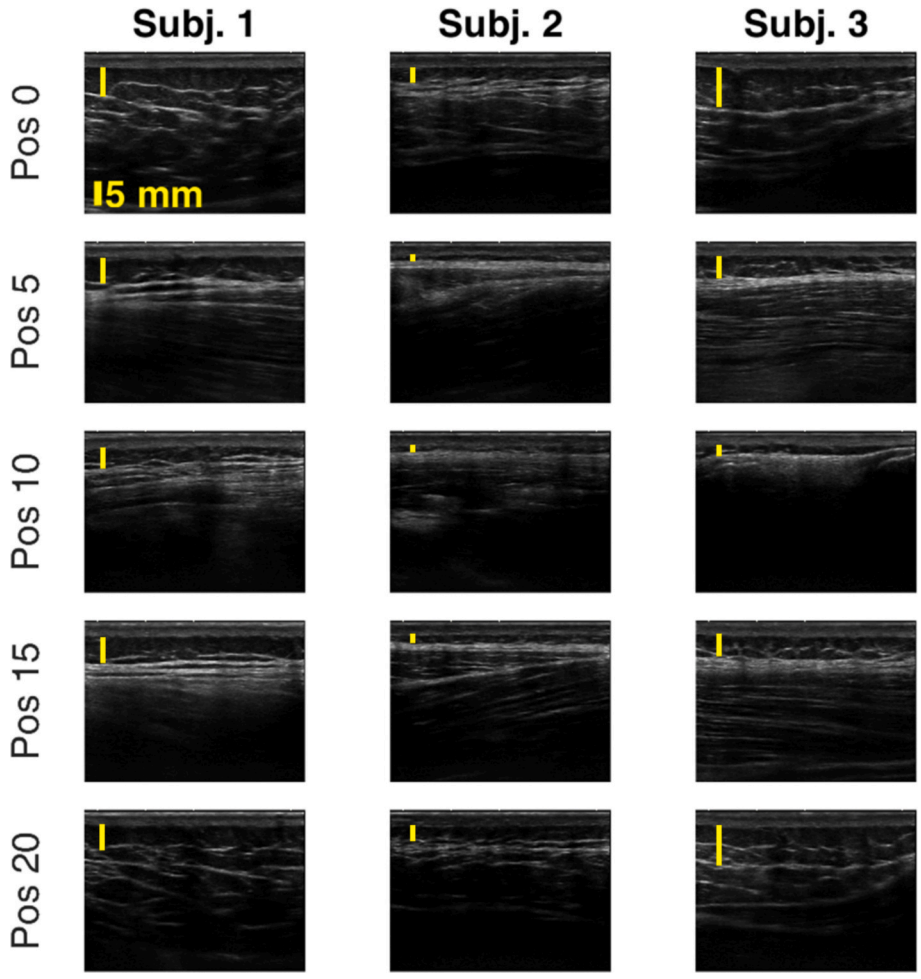

Fig. 6. US images of the 3 subjects (columns) at 5 symmetrical positions (rows) across the back with respect to the spine (position 10). Yellow lines show the thickness of the adipose layer.

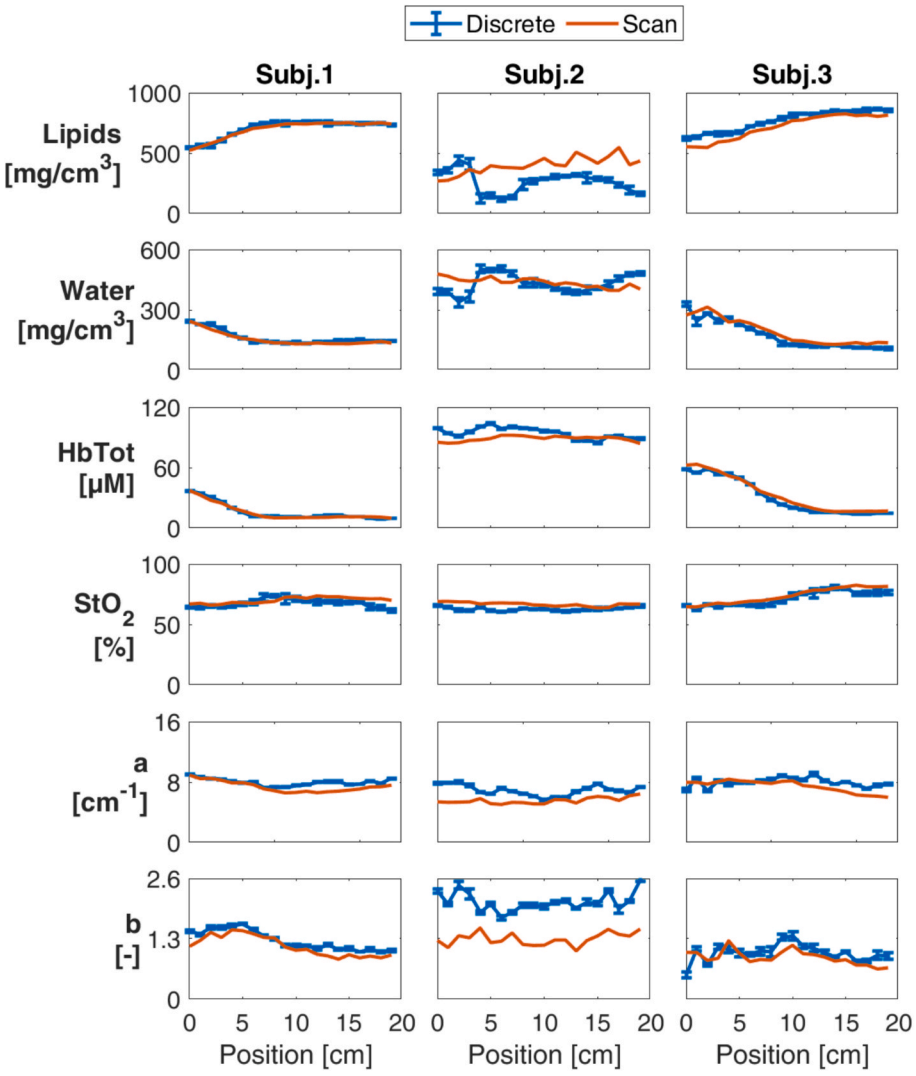

Fig. 7. Spatial variation of tissue composition for vertical *in vivo* measurements along the back. Columns correspond to different subjects and rows to constituent concentrations and scattering parameters. Error bars represent the standard deviation over 5 repetitions of discrete acquisitions.

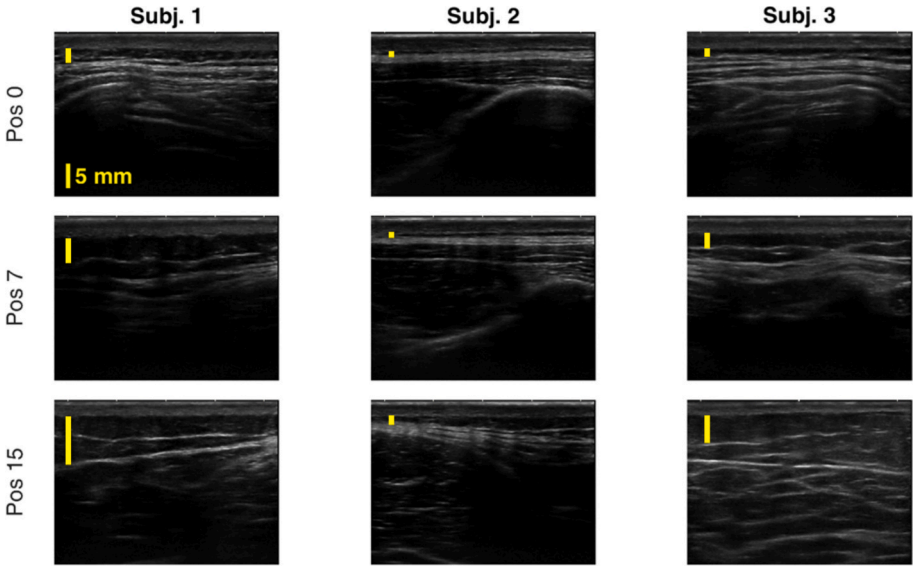

Fig. 8. US images of the 3 subjects (columns) at 3 positions (rows) along the back. Yellow lines show the thickness of the adipose layer.

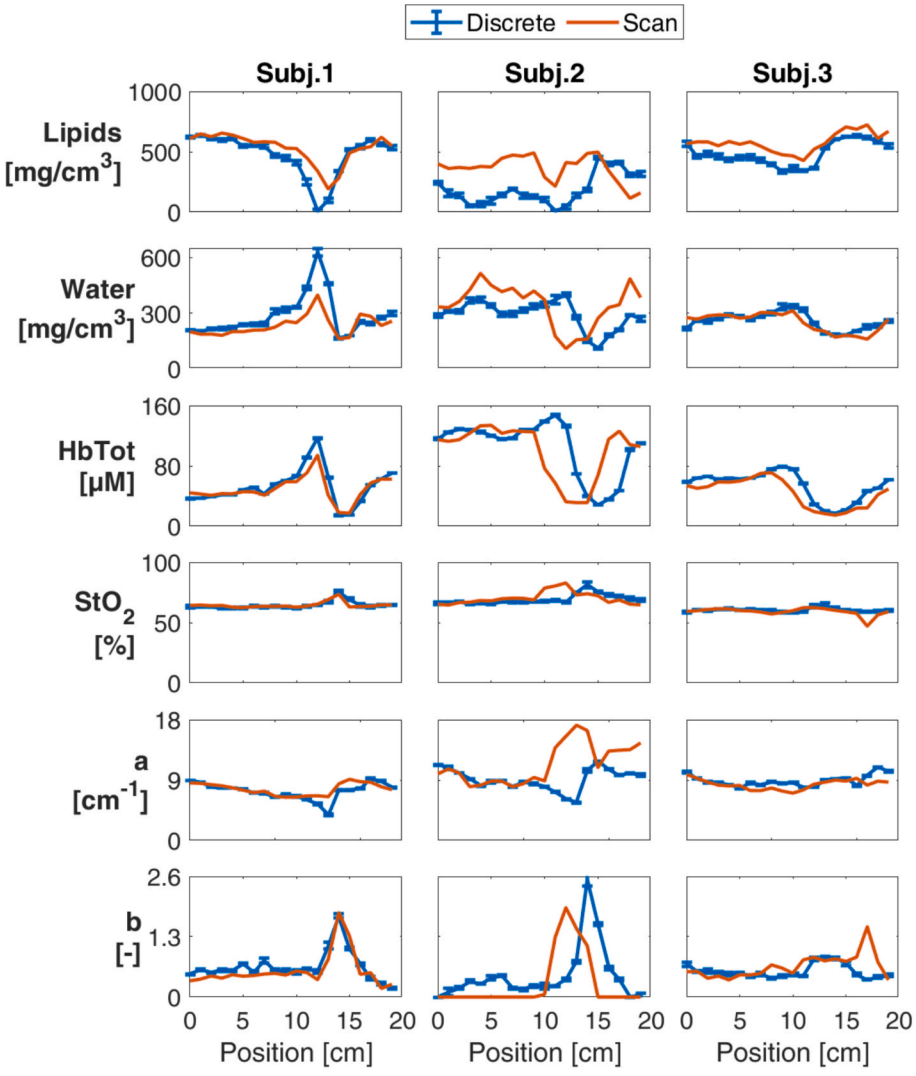

Fig. 9. Spatial variation of tissue composition for circular *in vivo* measurements around the calf. Columns correspond to different subjects and rows to constituent concentrations and scattering parameters. Error bars represent the standard deviation over 3 repetitions of discrete acquisitions.

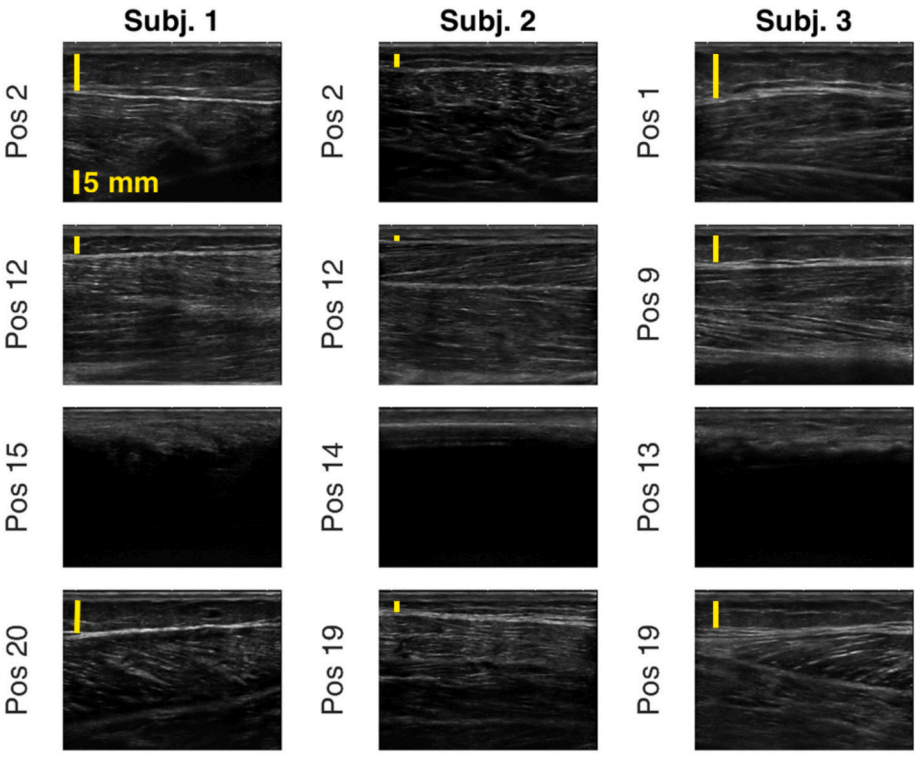

Fig. 10. US images of the 3 subjects (columns) at 4 positions (rows) around the calf. Yellow lines show the thickness of the adipose layer. The displayed positions are not the same for all subjects to adjust to tibia location (position 15, 14, 13) according to calf dimension.

of the tibia (positions 15, 14 and 13 respectively for subject 1, 2 and 3 in Fig. 10) consistently aligned among all constituents and scattering parameters. Contrary to what observed on the back (Fig. 5), now for all subjects (not only subject 2) bone is in contact with dermis, with no intermediate muscle layer. This causes an increase in lipids and oxygen saturation, concurrent with a reduction in water and hemoglobin. While absorption trends seem to be more affected by the intermediate layer, scattering reflects the proximity of bone, with an increase in slope in correspondence of spine and tibia.

5. Conclusions

In this work we introduced a parallel time domain diffuse optical spectroscopy system based on a compact 16-channel SiPM array. The overall footprint of the array board is 32 x 45 mm^2 and the single-photon timing resolution is 65 ps. The system was configured to parallelize the spectral acquisition over the 700–950 nm range, with spectral step $\Delta\lambda =$ 16 nm, thus matching significant absorption peaks of hemoglobin, lipids and the rising edge of water, that are characterizing components of muscle, adipose and bone tissue.

We applied the MEDPHOT protocol and observed excellent linearity ($R^2 = 0.9973$ for absorption and $R^2 = 0.9833$ for scattering as worst values), a negligible absorption–scattering coupling (an undesired deviation of 0.23 cm^{-1} in scattering for a 0.05 cm^{-1} change in absorption and negligible effect of scattering changes on estimated absorption), and a remarkable absorption accuracy (average error in absolute values of 3 %). Scattering tends to be overestimated (average error of + 17 %). The system demonstrated excellent reproducibility over 20 *in vivo* repositioning trials on the forearm, achieving a coefficient of variation (CV) < 5 % for absorption and < 4.5 % for scattering. Finally, scans were performed longitudinally and transversely along the back and around the calf of healthy volunteers to assess the system sensitivity to variations in tissue composition (lipids, water and hemoglobin) and microstructure (scattering parameters), including adipose tissue, muscle, and bone. The observed trends correlate well with complementary information from US imaging. The system effectively characterized tissue through smooth, continuous scans covering 20 cm in just 40 s.

At setup level, the main factors impacting on the quality of the experimental measurements are the limited spectral resolution (16 nm) and the use of a single attenuator to modulate light intensity over all the 16 channels. In other words, the accuracy of optical properties and constituent concentrations may improve (even if current values are already promising) by adding channels over the 700–950 nm range (thus reducing the band $\Delta\lambda$ of the single channel) and by means of power equalization (thus enabling a better control of the signal-to-noise ratio).

At measurement level, the main factors that impact on the scan quality are unwanted motion artifacts, different compression, vibrations, not perfectly straight scans. Misalignment between expected and actual probe position should also be considered. Now synchronization (to scan 20 cm in 40 s) is visually guided by the grid. Comparison between "discrete" and "continuous" measurements suggests that this method is efficient, but may be improved.

Future work will be devoted to test the effectiveness of the system during functional tasks (*e.g.*, breathing monitoring, brain activity tracking), thus exploiting at maximum the time advantage granted by the spectral parallelization with respect to a sequential approach. Also, we will deepen the re-arrangement of the 16 channels to obtain maps of the tissue that can be exploited for diagnostic applications not only through diffuse optics but also, *e.g.*, through autofluorescence imaging. Furthermore, research about SiPMs technology is rapid and unceasing, leveraging their cost-effectiveness, robustness and high responsivity. So, the use of larger area sensors up to 100 mm^2 [16] could grant higher dynamic range for broad source-detector distances, enhancing the investigation of deep tissue layers. Finally, so far we have maximized throughput within the single-photon statistics to focus on instrument validation. However, given the extremely short dead time of both the TCSPC board (650 ps) and the SiPM detectors (~4 ns), we plan to fully exploit the system capabilities by operating at count rates exceeding the single-photon statistics and applying appropriate algorithms to correct for the resulting pile-up effect [46]. This approach removes the need for

equalizing the signal across channels and will allow us to either increase the count rate, leading to an overall improvement in the signal-to-noise ratio, or, alternatively, to maintain the same signal-to-noise ratio while reducing the integration time, enabling the system to track fast dynamics more effectively.

CRediT authorship contribution statement

Elisabetta Avanzi: Writing – review & editing, Writing – original draft, Validation, Resources, Methodology, Investigation, Formal analysis, Conceptualization. **Giulia Maffeis:** Writing – review & editing, Writing – original draft, Visualization, Validation, Investigation, Formal analysis, Data curation. **Nicola Serra:** Writing – review & editing, Validation, Investigation. **Alessandro Bossi:** Writing – review & editing, Validation, Investigation. **Valerio Gandolfi:** Writing – review & editing, Resources. **Xinqiu Ye Lin:** Writing – review & editing, Resources. **Andrea Farina:** Writing – review & editing, Resources. **Cosimo D'Andrea:** Writing – review & editing, Resources. **Laura Di Sieno:** Writing – review & editing, Supervision, Resources, Methodology, Conceptualization. **Paola Taroni:** Writing – review & editing, Supervision, Methodology, Funding acquisition. **Antonio Pifferi:** Writing – review & editing, Supervision, Methodology, Funding acquisition, Conceptualization. **Alberto Dalla Mora:** Writing – review & editing, Supervision, Resources, Methodology, Funding acquisition, Conceptualization.

Declaration of competing interest

This work was partly funded by the National Plan for NRRP Complementary Investments (PNC, established with the decree-law 6 May 2021, n. 59, converted by law n. 101 of 2021) in the call for the funding of research initiatives for technologies and innovative trajectories in the health and care sectors (Directorial Decree n. 931 of 06–06-2022) – project n. PNC0000003 – CUP B53C22006720001 – AdvaNced Technologies for Human-centrEd Medicine (project acronym: ANTHEM), by the European Union's NextGenerationEU Programme with the I-PHOQS Infrastructure [IR0000016, ID D2B8D520, CUP B53C22001750006] "Integrated infrastructure initiative in Photonic and Quantum Sciences", by the European Union's NextGenerationEU Programme with PNRR – M4C2, investment 1.1 – "PRIN 2022 fund" – ALPHA [ID 2022HHZWRS, CUP D53D23013540006] and DIRS [ID 2022EB4B7E, CUP B53D23002530006].

Acknowlegdments

The authors express their gratitude to Fabio Motetta for having contributed to the work during his master thesis project.

Data availability

The experimental data described in this manuscript are available open access at the following reference: https://doi.org/10.5281/zenodo.14936939.

References

[1] T. Durduran, R. Choe, W. Baker, A.G. Yodh, *Diffuse Optics for Tissue monitoring and Tomography*, Reports Prog. Phys. 73 (2010) 076701, https://doi.org/10.1088/0034-4885/73/7/076701.

[2] A. Gibson, H. Dehghani, *Diffuse Optical Imaging*, Philos. Trans. R. Soc. a Math. Phys, Eng. Sci. 367 (2009) 3055, https://doi.org/10.1098/rsta.2009.0080.

[3] N. Mule, G. Maffeis, R. Cubeddu, C. Santangelo, G. Bianchini, P. Panizza, P. Taroni, *Monitoring of Neoadjuvant Chemotherapy through Time Domain Diffuse Optics: Breast Tissue Composition changes and Collagen Discriminative potential*, Biomed. Opt. Express 15 (2024) 4842, https://doi.org/10.1364/boe.527968.

[4] S.P. Poplack, E.Y. Park, K.W. Ferrara, *Optical Breast Imaging: a Review of Physical Principles, Technologies, and Clinical applications*, J. Breast Imaging 5 (2023) 520, https://doi.org/10.1093/jbi/wbad057.

[5] N. Bosschaart, S. Manohar, *ScienceDirect New Directions for Optical Breast Imaging and Sensing : Multimodal Cancer Imaging and Lactation Research*, Curr. Opin. Biomed. Eng. 22 (2022) 100380, https://doi.org/10.1016/j.cobme.2022.100380.

[6] N. Harnischmacher, E. Rodner, C.H. Schmitz, Detection of Breast Cancer Using Machine Learning on Time-Series Diffuse Optical Transillumination Data 29 (2024) 1, https://doi.org/10.1117/1.JBO.29.11.115001.

[7] C. Amendola, M. Buttafava, T. Carteano, L. Contini, L. Cortese, T. Durduran, L. Frabasile, C. N. Guadagno, U. Karadeniz, M. Lacerenza, J. Mesquida, S. Parsa, R. Re, D. Sanoja Garcia, S. Konugolu Venkata Sekar, L. Spinelli, A. Torricelli, A. Tosi, U. M. Weigel, M. A. Yaqub, M. Zanoletti, and D. Contini, *Assessment of Power Spectral Density of Microvascular Hemodynamics in Skeletal Muscles at Very Low and Low-Frequency via near-Infrared Diffuse Optical Spectroscopies*, Biomed. Opt. Express **14**, 5994 (2023), doi: 10.1364/BOE.502618.

[8] M.F. Bartlett, A.P. Oneglia, M.D. Ricard, A. Siddiqui, E.K. Englund, E.M. Buckley, D.M. Hueber, M.D. Nelson, *DCS Blood Flow Index Underestimates Skeletal Muscle Perfusion in Vivo: Rationale and Early evidence for the NIRS-DCS Perfusion Index*, J. Biomed. Opt. 29 (2024) 1, https://doi.org/10.1117/1.JBO.29.2.020501.

[9] C.A. Gómez, L. Brochard, E.C. Goligher, D. Rozenberg, W.D. Reid, D. Roblyer, *Combined Frequency Domain Near-Infrared Spectroscopy and Diffuse Correlation Spectroscopy System for Comprehensive Metabolic monitoring of Inspiratory Muscles during Loading*, J. Biomed. Opt. 29 (2024) 1, https://doi.org/10.1117/1.JBO.29.3.035002.

[10] Y. Matsuda, M. Nakabayashi, T. Suzuki, S. Zhang, M. Ichinose, Y. Ono, *Evaluation of Local Skeletal Muscle Blood Flow in Manipulative Therapy by Diffuse Correlation Spectroscopy*, Front. Bioeng. Biotechnol. 9 (2022) 1, https://doi.org/10.3389/fbioe.2021.800051.

[11] H. Ayaz, W. B. Baker, G. Blaney, D. A. Boas, H. Bortfeld, K. Brady, J. Brake, S. Brigadoi, E. M. Buckley, S. A. Carp, R. J. Cooper, K. R. Cowdrick, J. P. Culver, I. Dan, H. Dehghani, A. Devor, T. Durduran, A. T. Eggebrecht, L. L. Emberson, Q. Fang, S. Fantini, M. A. Franceschini, J. B. Fischer, J. Gervain, J. Hirsch, K. Hong, R. Horstmeyer, J. M. Kainerstorfer, T. S. Ko, D. J. Licht, A. Liebert, R. Luke, J. M. Lynch, J. Mesquida, R. C. Mesquita, N. Naseer, S. L. Novi, F. Orihuela-espina, T. D. O. Sullivan, D. S. Peterka, A. Pifferi, L. Pollonini, A. Sassaroli, R. Sato, F. Scholkmann, L. Spinelli, V. J. Srinivasan, S. Lawrence, I. Tachtsidis, Y. Tong, A. Torricelli, T. Urner, H. Wabnitz, M. Wolf, U. Wolf, S. Xu, C. Yang, A. G. Yodh, and M. A. Yücel, *Optical Imaging and Spectroscopy for the Study of the Human Brain : Status Report*, **9**, 1 (n.d.).

[12] J. Cao, T.J. Huppert, P. Grover, Enhanced Spatiotemporal Resolution Imaging of Neuronal Activity Using Joint Electroencephalography and Diffuse Optical Tomography 8 (2021) 1, https://doi.org/10.1117/1.NPh.8.1.015002.

[13] B. Kim, S. Zilpelwar, E.J. Sie, F. Marsili, B. Zimmermann, D.A. Boas, X. Cheng, *Measuring Human Cerebral Blood Flow and Brain Function with Fiber-based Speckle Contrast Optical Spectroscopy System*, Commun. Biol. 6 (2023) 1, https://doi.org/10.1038/s42003-023-05211-4.

[14] L. Contini, C. Amendola, D. Contini, A. Torricelli, L. Spinelli, R. Re, Detectability of Hemodynamic Oscillations in Cerebral Cortex through Functional near-Infrared Spectroscopy : A Simulation Study 11 (2024) 1, https://doi.org/10.1117/1.NPh.11.3.035001.

[15] A. Pifferi, M. Miniati, A. Farina, S. Konugolu Venkata Sekar, P. Lanka, A. Dalla Mora, G. Maffeis, and P. Taroni, *Initial Non-Invasive in Vivo Sensing of the Lung Using Time Domain Diffuse Optics*, Sci. Rep. **14**, 6343 (2024), doi: 10.1038/s41598-024-56862-0.

[16] L. Di Sieno, E. Avanzi, A. Behera, P. Levoni, F. Acerbi, A. Gola, L. Spinelli, A. Torricelli, A. Dalla Mora, *Breakthrough Light Harvesting in Time-Domain Diffuse Optics with 100 Mm2 Silicon Photomultiplier*, Opt. Laser Technol. 161 (2023) 109228, https://doi.org/10.1016/j.optlastec.2023.109228.

[17] E. Avanzi, V. Gandolfi, A. Costa, A. Ghezzi, N. Lusardi, F. Garzetti, E. Ronconi, G. Bonanno, A. Geraci, C. D'Andrea, A. Farina, A. Dalla Mora, L. Di Sieno, *High-Throughput Wide-Field Multispectral FLIM System based on a 16-Channel Silicon Photomultiplier Array*, APL Photonics 10 (2025), https://doi.org/10.1063/5.0254427.

[18] L. Di Sieno, A. Behera, S. Rohilla, E. Ferocino, D. Contini, A. Torricelli, B. Krämer, F. Koberling, A. Pifferi, A. Dalla Mora, *Probe-Hosted Large Area Silicon Photomultiplier and High-Throughput timing Electronics for Enhanced Performance Time-Domain Functional near-Infrared Spectroscopy*, Biomed. Opt. Express 11 (2020) 6389, https://doi.org/10.1364/BOE.400868.

[19] R. Georgel, K. Grygoryev, S. Sorensen, H. Lu, S. Andersson-Engels, R. Burke, D. O'Hare, *Silicon Photomultiplier—A High Dynamic Range, High Sensitivity Sensor for Bio-Photonics applications*, Biosensors 12 (2022) 793, https://doi.org/10.3390/bios12100793.

[20] V.J. Kitsmiller, T.D. O'Sullivan, *Next-Generation Frequency Domain Diffuse Optical Imaging Systems using Silicon Photomultipliers*, Opt. Lett. 44 (2019) 562, https://doi.org/10.1364/OL.44.000562.

[21] R. Re, L. Spinelli, F. Martelli, L. Di Sieno, I. Bargigia, C. Amendola, G. Maffeis, A. Torricelli, *A Review on Time Domain Diffuse Optics: Principles and applications on Human Biological Tissues*, La Riv. Del Nuovo Cim. (2025), https://doi.org/10.1007/s40766-025-00067-2.

[22] Y. Ueda, T. Yamanaka, D. Yamashita, T. Suzuki, E. Ohmae, M. Oda, Y. Yamashita, *Reflectance Diffuse Optical Tomography: its Application to Human Brain Mapping*, Japanese J. Appl. Physics, Part 2 Lett. 44 (2005), https://doi.org/10.1143/JJAP.44.L1203.

[23] H. Zhao, F. Gao, Y. Tanikawa, Y. Yamada, *Time-Resolved Diffuse Optical Tomography and its Application to in Vitro and in Vivo Imaging*, J. Biomed. Opt. 12 (2007) 062107, https://doi.org/10.1117/1.2815724.

[24] H. Zhao, R.J. Cooper, *Review of recent Progress toward a Fiberless*, Whole-Scalp Diffuse Optical Tomography System, Neurophotonics 5 (2017) 1, https://doi.org/10.1117/1.nph.5.1.011012.
[25] W. Chen, B. Wang, H. Zhao, F. Gao, *Lock-in-Photon-Counting-based Highly-Sensitive and Large-Dynamic Imaging System for Diffuse Optical Tomography*, Opt. Infobase Conf. Pap. 7 (2016) 448, https://doi.org/10.1364/TRANSLATIONAL.2016.JTu3A.24.
[26] Y. Bérubé-Lauzière, M. Crotti, S. Boucher, S. Ettehadi, J. Pichette, I. Rech, *Prospects on Time-Domain Diffuse Optical Tomography based on Time-Correlated Single Photon counting for Small Animal Imaging*, J. Spectrosc. 2016 (2016), https://doi.org/10.1155/2016/1947613.
[27] S.V. Panasyuk, S. Yang, D.V. Faller, D. Ngo, R.A. Lew, J.E. Freeman, A.E. Rogers, *Medical Hyperspectral Imaging to Facilitate Residual Tumor Identification during Surgery*, Cancer Biol. Ther. 6 (2007) 439, https://doi.org/10.4161/cbt.6.3.4018.
[28] L.L. De Boer, T.M. Bydlon, F. Van Duijnhoven, M.J.T.F.D. Vranken Peeters, C. E. Loo, G.A.O. Winter-Warnars, J. Sanders, H.J.C.M. Sterenborg, B.H.W. Hendriks, T.J.M. Ruers, *Towards the use of Diffuse Reflectance Spectroscopy for Real-Time in Vivo Detection of Breast Cancer during Surgery*, J. Transl. Med. 16 (2018) 1, https://doi.org/10.1186/s12967-018-1747-5.
[29] H. Vavadi, A. Mostafa, F. Zhou, K.M.S. Uddin, M. Althobaiti, C. Xu, R. Bansal, F. Ademuyiwa, S. Poplack, Q. Zhu, *Compact Ultrasound-Guided Diffuse Optical Tomography System for Breast Cancer Imaging*, J. Biomed. Opt. 24 (2018) 1, https://doi.org/10.1117/1.JBO.24.2.021203.
[30] A. Sudakou, F. Lange, H. Isler, P. Lanka, S. Wojtkiewicz, P. Sawosz, D. Ostojic, M. Wolf, A. Pifferi, I. Tachtsidis, A. Liebert, A. Gerega, *Time-Domain NIRS System based on Supercontinuum Light Source and Multi-Wavelength Detection: Validation for Tissue Oxygenation Studies*, Biomed. Opt. Express 12 (2021) 6629, https://doi.org/10.1364/boe.431301.
[31] Q. Pian, R. Yao, L. Zhao, X. Intes, *Hyperspectral Time-Resolved Wide-Field Fluorescence Molecular Tomography based on Structured Light and Single-Pixel Detection*, Opt. Lett. 40 (2015) 431, https://doi.org/10.1364/ol.40.000431.
[32] A. Bassi, J. Swartling, C. D'Andrea, A. Pifferi, A. Torricelli, R. Cubeddu, *Time-Resolved Spectrophotometer for Turbid Media based on Supercontinuum Generation in a Photonic Crystal Fiber*, Opt. Lett. 29 (2004) 2405, https://doi.org/10.1364/ol.29.002405.
[33] A. Gerega, D. Milej, W. Weigl, M. Kacprzak, A. Liebert, *Multiwavelength Time-Resolved near-Infrared Spectroscopy of the Adult Head: Assessment of Intracerebral and Extracerebral Absorption changes*, Biomed. Opt. Express 9 (2018) 2974, https://doi.org/10.1364/boe.9.002974.
[34] F. Lange, L. Giannoni, I. Tachtsidis, *The use of Supercontinuum Laser sources in Biomedical Diffuse Optics: Unlocking the Power of Multispectral Imaging*, Appl. Sci. 11 (2021), https://doi.org/10.3390/app11104616.
[35] F. Lange, F. Peyrin, B. Montcel, *Broadband Time-Resolved Multi-Channel Functional near-Infrared Spectroscopy System to Monitor in Vivo Physiological changes of Human Brain activity*, Appl. Opt. 57 (2018) 6417, https://doi.org/10.1364/ao.57.006417.
[36] O. Jarlman, R. Berg, S. Andersson-Engels, S. Svanberg, H. Pettersson, *Time-Resolved White Light Transillumination for Optical Imaging*, Acta Radiol. 38 (1997) 185, https://doi.org/10.1080/02841859709171266.
[37] R. Nachabé, B.H.W. Hendriks, M. Van Der Voort, E. Adrien, H.J.C.M. Sterenborg, Estimation of Biological Chromophores Using Diffuse Optical Spectroscopy : Benefit of Extending the UV-VIS Wavelength Range to 18 (2010) 879. Include 1000 to 1600 Nm.
[38] S. Konugolu Venkata Sekar, A. Dalla Mora, I. Bargigia, E. Martinenghi, C. Lindner, P. Farzam, M. Pagliazzi, T. Durduran, P. Taroni, A. Pifferi, and A. Farina, Broadband (600–1350 Nm) Time-Resolved Diffuse Optical Spectrometer for Clinical Use, IEEE J. Sel. Top. Quantum Electron. 22, 406 (2016), doi: 10.1109/JSTQE.2015.2506613.
[39] A. Pifferi, A. Torricelli, A. Bassi, P. Taroni, R. Cubeddu, H. Wabnitz, D. Grosenick, M. Möller, R. Macdonald, J. Swartling, T. Svensson, S. Andersson-Engels, R.L. P. van Veen, H.J.C.M. Sterenborg, J.-M. Tualle, H.L. Nghiem, S. Avrillier, M. Whelan, H. Stamm, *Performance Assessment of Photon Migration Instruments: the MEDPHOT Protocol*, Appl. Opt. 44 (2005) 2104, https://doi.org/10.1364/AO.44.002104.
[40] F. Martelli, S. Del Bianco, A. Ismaelli, and G. Zaccanti, *Light Propagation through Biological Tissue and Other Diffusive Media: Theory, Solutions, and Software* (SPIE, 1000 20th Street, Bellingham, WA 98227-0010 USA, 2009).
[41] P. Lanka, L. Yang, D. Orive-Miguel, J.D. Veesa, S. Tagliabue, A. Sudakou, S. Samaei, M. Forcione, Z. Kovacsova, A. Behera, T. Gladytz, D. Grosenick, L. Hervé, T. Durduran, K. Bejm, M. Morawiec, M. Kacprzak, P. Sawosz, A. Gerega, A. Liebert, A. Belli, I. Tachtsidis, F. Lange, G. Bale, L. Baratelli, S. Gioux, K. Alexander, M. Wolf, S.K.V. Sekar, M. Zanoletti, I. Pirovano, M. Lacerenza, L. Qiu, E. Ferocino, G. Maffeis, C. Amendola, L. Colombo, L. Frabasile, P. Levoni, M. Buttafava, M. Renna, L. Di Sieno, R. Re, A. Farina, L. Spinelli, A. Dalla Mora, D. Contini, P. Taroni, A. Tosi, A. Torricelli, H. Dehghani, H. Wabnitz, A. Pifferi, *Multi-Laboratory Performance Assessment of Diffuse Optics Instruments: the BitMap Exercise*, J. Biomed. Opt. 27 (2022) 1, https://doi.org/10.1117/1.JBO.27.7.074716.
[42] L. Di Sieno, D. Contini, G. Lo Presti, L. Cortese, T. Mateo, B. Rosinski, E. Venturini, P. Panizza, M. Mora, G. Aranda, M. Squarcia, A. Farina, T. Durduran, P. Taroni, A. Pifferi, A. Dalla Mora, *Systematic Study of the effect of Ultrasound Gel on the Performances of Time-Domain Diffuse Optics and Diffuse Correlation Spectroscopy*, Biomed. Opt. Express 10 (2019) 3899, https://doi.org/10.1364/BOE.10.003899.
[43] C. D'Andrea, L. Spinelli, A. Bassi, A. Giusto, D. Contini, J. Swartling, A. Torricelli, R. Cubeddu, *Time-Resolved Spectrally Constrained Method for the Quantification of Chromophore Concentrations and Scattering Parameters in Diffusing Media*, Opt. Express 14 (2006) 1888, https://doi.org/10.1364/OE.14.001888.
[44] X. Wang, B.W. Pogue, S. Jiang, X. Song, K.D. Paulsen, C.A. Kogel, S.P. Poplack, W. A. Wells, *Approximation of Mie Scattering Parameters in Near-Infrared Tomography of Normal Breast Tissue in Vivo*, J. Biomed. Opt. 10 (2005) 051704, https://doi.org/10.1117/1.2098607.
[45] M. A. Bredella, Sex Differences in Body Composition, in Sex and Gender Factors Affecting Metabolic Homeostasis, Diabetes and Obesity. Advances in Experimental Medicine and Biology (Springer, Cham, 2017), pp. 9–27 , doi:10.1007/978-3-319-70178-3_2.
[46] E. Avanzi, A. Behera, D. Contini, L. Spinelli, A. Dalla Mora, L. Di Sieno, *Effects and Correctability of Pile-up Distortion using established figures of Merit in Time-Domain Diffuse Optics at Extreme Photon rates*, Sci. Rep. 12 (2022) 5417, https://doi.org/10.1038/s41598-022-09385-5.